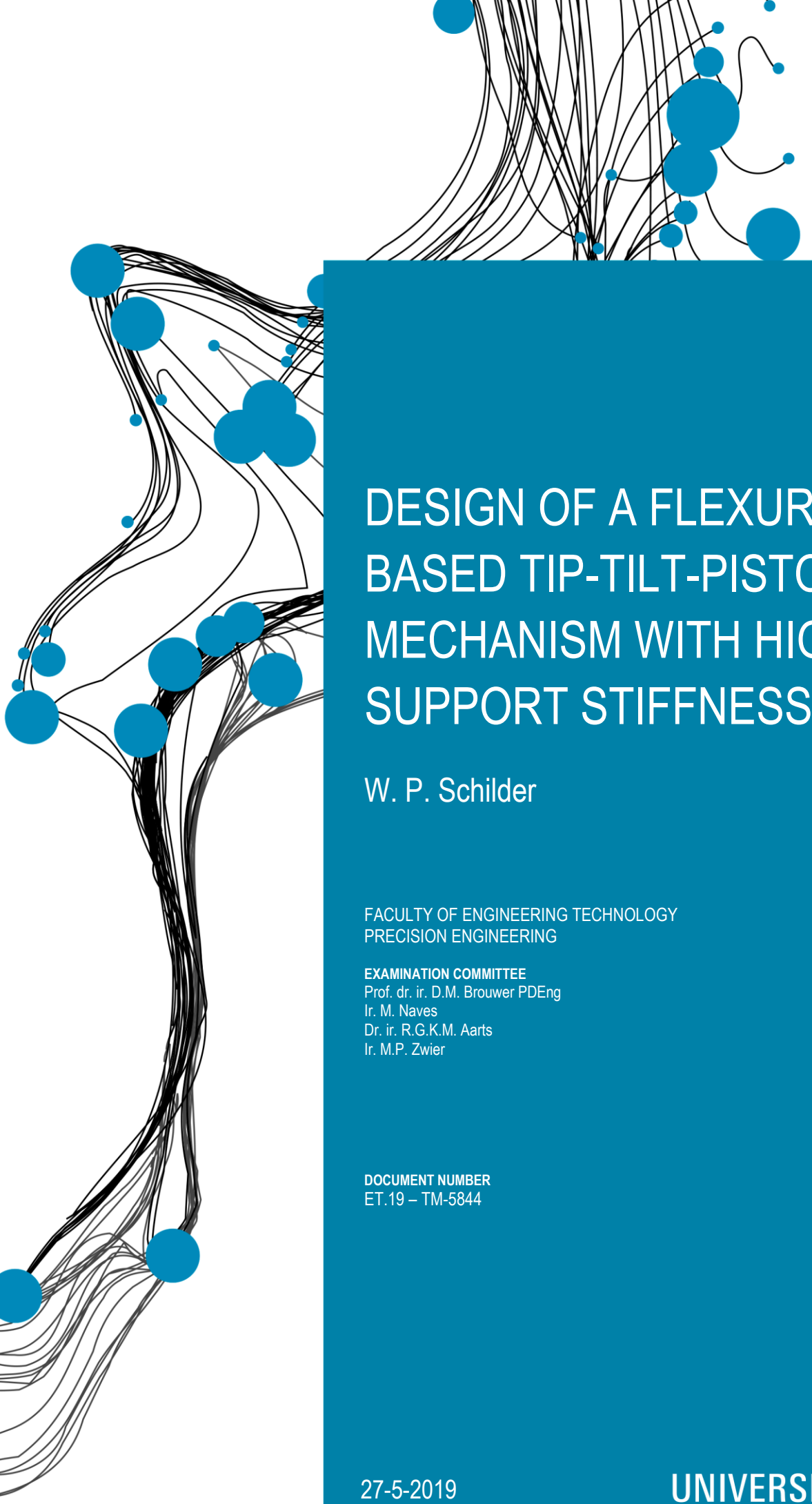

DESIGN OF A FLEXURE-BASED TIP-TILT-PISTON MECHANISM WITH HIGH SUPPORT STIFFNESS

W. P. Schilder

FACULTY OF ENGINEERING TECHNOLOGY
PRECISION ENGINEERING

EXAMINATION COMMITTEE
Prof. dr. ir. D.M. Brouwer PDEng
Ir. M. Naves
Dr. ir. R.G.K.M. Aarts
Ir. M.P. Zwier

DOCUMENT NUMBER
ET.19 – TM-5844

27-5-2019

UNIVERSITY OF TWENTE.

ET.19/TM-5844

DESIGN OF A FLEXURE-BASED TIP-TILT-PISTON MECHANISM WITH HIGH SUPPORT STIFFNESS

Wout P. Schilder
Faculty of Eningeering Technology
University of Twente P.O. Box 217
7500AE Enschede, The Netherlands
Email: w.p.schilder@student.utwente.nl

ABSTRACT

Flexure based Tip-Tilt-Piston (TTP) mechanisms are often found in optical applications like micro mirror arrays or large fast steering mirrors. In this paper the design of a new TTP mechanism with a high support stiffness over a translational stroke of $\pm$ 4 mm and a rotational stroke of $\pm$ 0.04 rad is presented. Parametric models of multiple concepts with various levels of complexity are generated. By means of optimization a necessary support stiffness is enforced while the actuation stiffness is minimized. During shape optimization penalty constraints are applied to the parasitic eigenfrequencies, occurring stress and support stiffness drop. Analytic and flexible multi-body modelling approaches are used for efficient function evaluations in the optimization algorithm. Additional efficiency is gained by exploiting symmetry in the concepts and choosing an optimal test trajectory. For validation of the results, finite element analyses are conducted. This resulted in a design with an eigenfrequency of 31 Hz corresponding to tip-tilt motion and 15 Hz for piston motion. The first parasitic eigenfrequency corresponding to support stiffness is found at 734 Hz for a payload of 1 kg.

INTRODUCTION

For applications where high accuracy and repeatability is required, flexure-based mechanisms are often used as they do not suffer from hysteresis, backlash and friction. Furthermore, flexure-based mechanisms are virtually maintenance free [1] [2] and require no lubrication. Therefore, they are applicable in vacuum since there is no contamination or vaporisation from lubricants which makes them suitable for typical high performance optical applications.

Tip-Tilt-Piston (TTP) mechanisms are mostly found in mirror steering applications on different scales. They provide two rotational Degrees of Freedom (DoF) and one translational DoF perpendicular to the tip-tilt rotation axes. On a micro-scale, TTP mechanisms are found in micro-mirror arrays. The DoFs are enabled by Inverted Series Connected (ISC) actuators which results in a fully planar mechanism [3] [4]. Larger TTP mechanisms are found in Fast Steering Mirror (FSM) applications [5]. These and other [6] are typically driven by piezoelectric actuators, yielding high support stiffness but limited range of motion. A relatively high range of motion mechanism is described by Pernette et al. [7] However, no stiffness properties are mentioned. Hao et al. [8] designed a fully monolithic flexure based TTP mechanism. However, it is also limited to a small range of motion.

In this paper, a large range of motion TTP mechanism is proposed which allows for high support stiffness over the full range of motion. To allow for this large range of motion, a new TTP mechanism is proposed consisting of radially oriented flexures.

Based on a set of requirements, three different concepts with a number of sub-concepts are presented. By means of analytic modelling and Nelder-Mead optimization dimensions of the concepts are determined. Based on the optimization results, a TTP mechanism is designed and validated by using Finite Element Methods.

REQUIREMENTS

A given end-effector which is rotationally symmetric around the z-axis is illustrated in Fig. 1. This end-effector must be suspended by means of flexible elements. The leaf springs are connected to the end-effector on a radius r_0 of 20 mm. The inertia properties of the end-effector are listed in Table 1. The tip of the end-effector has a desired cylindrical workspace with a ra-

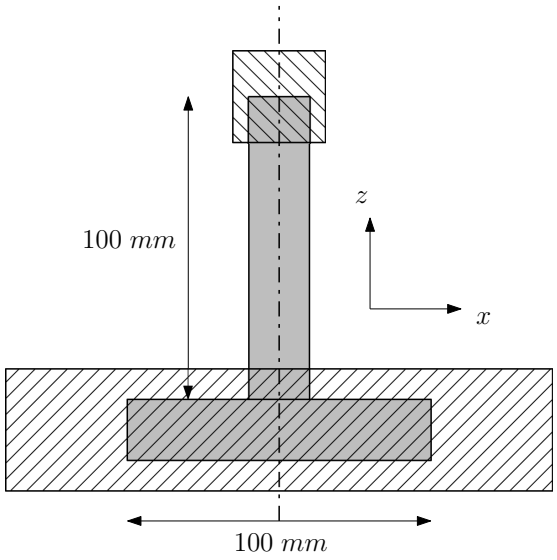

FIGURE 1: end-effector

TABLE 1: Boundary conditions

Parameter	value	unit
u_z	± 4	mm
θ_x, θ_y	± 0.04	rad
r_0	20	mm
M	1	kg
I_{xx}, Iyy	$1 \cdot 10^{-3}$	kgm^2
I_{zz}	$1.1 \cdot 10^{-3}$	kgm^2
K_x, K_y	$3 \cdot 10^7$	N/m
K_z	$3 \cdot 10^4$	N/m
K_{rx}, K_{ry}	12	Nm/rad
K_{rz}	$2 \cdot 10^4$	Nm/rad

dius of 4 mm and a height of 8 mm, illustrated as the top hatched surface in Fig. 1. At rest the end-effector is in the centre of the workspace. To span the entire workspace a piston stroke in z-direction of $\pm$ 4 mm and a tip-tilt rotation in the xy-plane of $\pm$ 0.04 rad are required, since the shaft has a length of 100 mm. For any stroke within the workspace a maximum drive stiffness and a minimum support stiffness is defined, listed in Table 1. As an additional requirement, the support stiffness in the xy-plane may drop no more than 50% during any stroke. Internal eigenfrequencies that do not concern motion of the end-effector (ω^i) must be above 250 Hz.

On the bottom flange three voice coil motors evenly distributed on a pitch circle will drive the mechanism. The build volume is defined as a cuboid with dimensions 300 x 300 x 50 mm in x-, y- and z-direction respectively, represented by the bottom hatched surface in Fig. 1.

The most favourable design is an exact constraint mechanism. To achieve this, the Freedom and Constraint Topology method by Hopkins et al. [9] is used. Tip-tilt motion requires that all rotation axes in the xy-plane are free, which is illustrated by a planar square freedom space in Fig. 2a. Translational piston motion can be emulated by a rotation around an axis at infinite distance. This is visualized as the hoop in Fig. 2a. The complementary constraint space is illustrated in Fig. 2b as three constraint lines on the xy-plane. The constraint lines indicate directions for which translation is fixed.

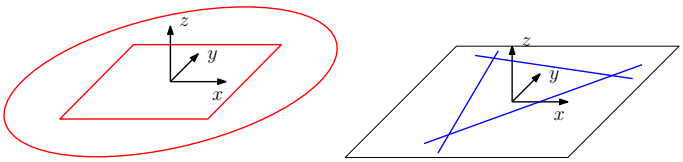

(a) (b)

FIGURE 2: (a) Freedom space. (b) Constraint space.

Centre of Compliance

The compliance matrix C of a mechanism is defined as:

$$\begin{Bmatrix} U \\ R \end{Bmatrix} = C \begin{Bmatrix} F \\ M \end{Bmatrix} \tag{1}$$

If the compliance matrix is diagonal, no coupling between rotations R and forces F or translations U and moments M occurs. In this case the compliance matrix is evaluated in the centre of compliance, which does not necessarily exist for every spatial mechanism. The absence of coupling terms is advantageous because it reduces pivot shift and could reduce the total driving stiffness. Symmetric systems are more likely to have a centre of compliance [1], which is therefore required. A typical symmetric design that satisfies the constraint space is found in Fig. 3. It consists of three folded leaf springs which are interconnected at the centre. A folded leaf spring has a single constraint line that is collinear with the fold line [1].

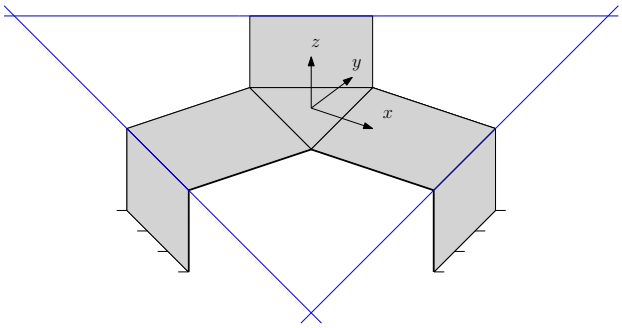

FIGURE 3: Concept 1a.

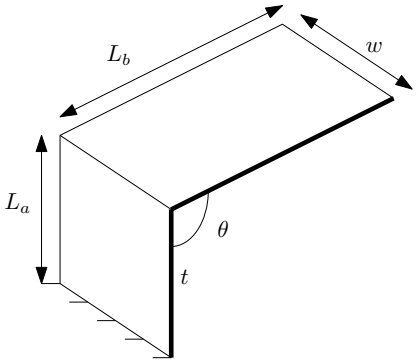

FIGURE 4: Analytic model variables

METHOD

In this section the design, modelling and optimization strategy is explained. First, an analytical model for the undeflected state of a folded leaf spring is presented to analyse and understand the concept in Fig. 3. Thereafter, modelling and analysis of more complex concepts with multi-body software is explained. For shape optimization of the multi-body models objectives and constraints are presented.

Analytical Model

For a better understanding of a folded leaf spring, an analytic model is generated. Previously Van Eijk [10] proposed equations for the compliance of a folded leaf spring in equilibrium position, where loads are applied at the fold. In this section a new model is introduced that also takes shear, in-plane bending and warping into account. The model is presented as a compliance matrix which is evaluated at the free end of the folded leaf spring. Twelve unique compliance values have to be found that depend on Elongation, Bending, Torsion, Warping and Shear. The variables for this model are shown in Fig. 4. In the next sections the compliance terms for each deformation mode are presented. For the plots and validations, the following dimensions are used:

$$
\begin{aligned}
L_a &= 50mm \\
L_b &= 50mm \\
w &= 40mm \\
t &= 0.50mm \\
\theta &= \pi/3rad
\end{aligned}
$$

Elongation. The compliance matrix for elongation has the following form.

$$
C_{elongation} = \begin{bmatrix}
\frac{L_a+L_a\cos^2\theta}{EA} & 0 & -\frac{L_a}{EA}\sin\theta\cos\theta & 0 & 0 & 0 \\
 & 0 & 0 & 0 & 0 & 0 \\
 & & \frac{L_a\sin^2\theta}{EA} & 0 & 0 & 0 \\
 & & & 0 & 0 & 0 \\
 & Symm. & & & 0 & 0 \\
 & & & & & 0
\end{bmatrix} \tag{2}
$$

Bending. The compliance for in-plane and out-of-plane bending is found using the beam deflection formulas for cantilever beams with an end force or end moment. The out-of-plane and in-plane bending compliance matrices can be found in Eqs. (3) and (4) respectively.

Torsion & Warping. Since the DoFs are strongly dependent on torsion and the leaf springs are expected to be short and wide, the effects of constrained warping have to be taken into account [22]. The analytic expression is found by solving a system of differential equations for ϕ as found in the following equation by Vlasov [11].

$$
EI_w \frac{d^4\phi}{dx^4} - GJ\frac{d^2\phi}{dx^2} = m_x \tag{5}
$$

In this equation I_w is the warping constant as given in Eq. (6) for a rectangular cross section and m_x is a distributed torque along the length of the beam.

$$
I_w = \frac{w^3t^3}{144} \tag{6}
$$

Because the torsional moment is constant along the entire beam, the expression for the total torsional moment in Eq. (7) can be

used

$$-EI_w\frac{d^3\phi}{dx^3}+GJ\frac{d\phi}{dx}=M \tag{7}$$

This equation is rewritten to:

$$-\frac{1}{\lambda^2}\frac{d^3\phi}{dx^3}+\frac{d\phi}{dx}=\frac{M}{St} \tag{8}$$

Where

$$St=GJ \tag{9}$$

$$\lambda=\sqrt{\frac{St}{EI_w}} \tag{10}$$

The folded leaf spring is modelled as two separate beams which are coupled by the boundary conditions in Eq. (11). The leaf spring is clamped on one end ($\phi_1(0)=0$) and warping (ϕ') is constrained at both ends. The twist angle ϕ is transferred depending on the fold θ angle as illustrated in Fig. 5. Warping ϕ' and Bi-moment B are transferred regardless of the fold angle.

$$\begin{aligned}
\phi_1(0)&=0\\
\phi_1'(0)&=0\\
\phi_1(L_a)&=-\phi_2(L_a)/\cos\theta\\
\phi_1'(L_a)&=\phi_2'(L_a)\\
B_1(L_a)&=B_2(L_a)\\
\phi_2'(L_a+L_a)&=0
\end{aligned} \tag{11}$$

The compliance matrix in Eq. (12) shows the nonzero terms that occur due to torsion.

$$C_{torsion}=\begin{bmatrix}
0 & 0 & 0 & 0 & 0 & 0\\
 & C_{raMz}L_b^2\sin\theta & 0 & C_{rbMz}L_b & 0 & C_{raMz}L_b\sin\theta\\
 & & 0 & 0 & 0 & 0\\
 & & & C_{rbMx} & 0 & C_{rbMz}\\
 & Symm. & & & 0 & 0\\
 & & & & & C_{raMz}\sin\theta
\end{bmatrix} \tag{12}$$

To obtain the compliance expressions, the following systems of equations have to be solved.

$$\begin{aligned}
\begin{bmatrix}-\frac{1}{\lambda^2}\frac{d^3\phi_1}{dx^3}+\frac{d\phi_1}{dx}\\ -\frac{1}{\lambda^2}\frac{d^3\phi_2}{dx^3}+\frac{d\phi_2}{dx}\end{bmatrix}&=\begin{bmatrix}\frac{-\cos\theta Mx}{St}\\ \frac{Mx}{St}\end{bmatrix}\\
\begin{bmatrix}-\frac{1}{\lambda^2}\frac{d^3\phi_1}{dx^3}+\frac{d\phi_1}{dx}\\ -\frac{1}{\lambda^2}\frac{d^3\phi_2}{dx^3}+\frac{d\phi_2}{dx}\end{bmatrix}&=\begin{bmatrix}\frac{\sin\theta Mz}{St}\\ 0\end{bmatrix}
\end{aligned} \tag{13}$$

$$C_{aop}=\begin{bmatrix}
\frac{L_a^3\sin^2\theta}{3EI} & 0 & \frac{L_a^2(L_a\sin 2\theta-3*L_b\sin\theta}{6EI} & 0 & \frac{L_a^2\sin\theta}{2EI} & 0\\
 & 0 & 0 & 0 & 0 & 0\\
 & & \frac{L_a^3\cos^2\theta+3L_b^2L_a+L_b^3-3L_bL_a^2\cos^2\theta}{3EI} & 0 & -\frac{L_b^2+2L_bL_a-L_a^2\cos\theta}{2EI} & 0\\
 & & & 0 & 0 & 0\\
 & Symm. & & & \frac{L_b+L_a}{EI} & 0\\
 & & & & & 0
\end{bmatrix} \tag{3}$$

$$C_{ip}=\begin{bmatrix}
0 & 0 & 0 & 0 & 0 & 0\\
 & \frac{L_b^3+L_a^3-3L_bL_a^2\cos\theta+3La^2L_a\cos^2\theta}{3EI_{ip}} & 0 & -\frac{L_a^2\sin\theta-L_bL_a\sin 2\theta}{2EI_{ip}} & 0 & \frac{L_b^2-L_a^2\cos\theta+2L_bL_a\cos^2\theta}{2EI_{ip}}\\
 & & 0 & 0 & 0 & 0\\
 & & & \frac{L_a\sin^2\theta}{EI_{ip}} & 0 & \frac{L_a\cos\theta\sin\theta}{EI_{ip}}\\
 & Symm. & & & 0 & 0\\
 & & & & & \frac{L_b+L_a\cos^2\theta}{EI_{ip}}
\end{bmatrix} \tag{4}$$

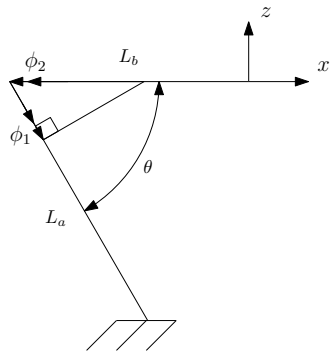

FIGURE 5: Propagation of twist angle through a fold

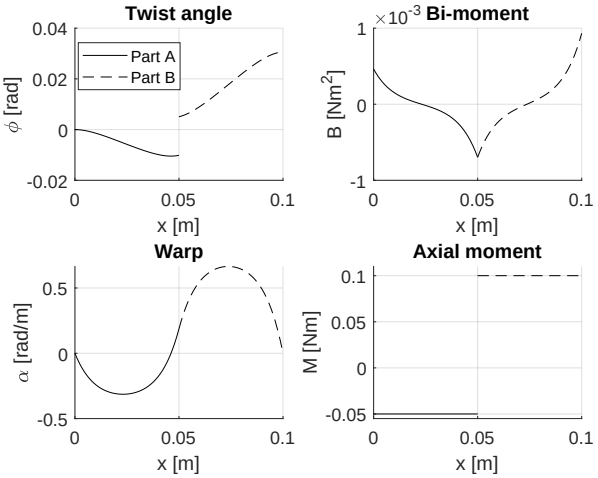

FIGURE 6: Torsion plots for $\theta = 60°$

By taking the derivative of the solutions to their corresponding input torque, the compliance is found.

$$\begin{aligned} C_{rbMx} &= \frac{\phi_2}{M_x} \\ C_{rbMz} &= \frac{\phi_2}{M_z} \\ C_{raMz} &= \frac{\phi_1}{M_z} \end{aligned} \tag{14}$$

In Fig. 6 the propagation of the twist angle, warping, bi-moment and axial moment can be found for a folded leaf spring. A torque of 0.1 Nm is applied at the free end and a fold angle of 60° is applied. The plotted values are evaluated in the local coordinate systems of the leaf spring segments, where the x-axis is parallel to the leaf spring.

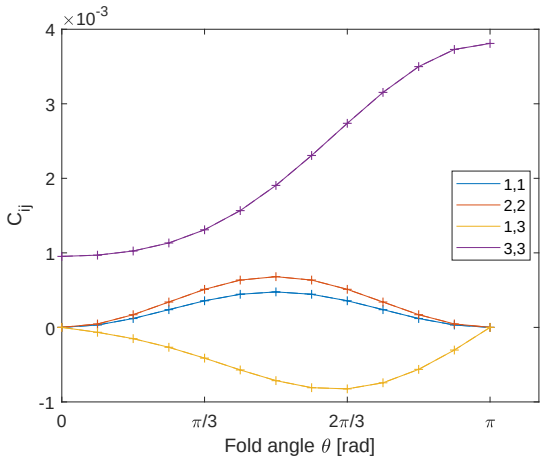

FIGURE 7: Translational compliance matrix values

Shear. Compliance caused by shear effects are defined by Eq. (15) where k is the shear correction factor which is given by Cowper [12]. For rectangular cross sections k is equal to 0.85.

$$C_s = \frac{L}{GAk} \tag{15}$$

The compliance matrix for shear effects can be found in Eq. (16)

$$C_{shear} = \begin{bmatrix} 0 & 0 & 0\,0\,0 & 0 \\ \frac{L_a+L_a}{GAk} & & 0\,0\,0 & 0 \\ & & 0\,0\,0 & 0 \\ & & 0\,0 & 0 \\ Symm. & & 0 & 0 \\ & & & \frac{L_a}{GAkL_a} \end{bmatrix} \tag{16}$$

Validation of the compliance matrix. The total compliance matrix of a single folded leaf spring is created by adding all previously presented matrices. To validate that the model is accurate, it is compared with Multi-Body analysis software SPACAR. In Figs. 7 and 8 the largest compliance values for translation and rotation are plotted for the fold angle θ. The + markers indicate the values obtained from the analytic model. For 98% of the values found, the difference of between the analytical model and spacar is less than 1%.

Stress. To find dimensions by optimization, the stress must be known to constrain the optimization algorithm. An expression for bending stress in a folded leaf spring is given by Soemers [1]. However, these equations do not take the fold angle into account. Therefore, the bending stress due to a deformation in z-direction is calculated using the Beam Constraint Model

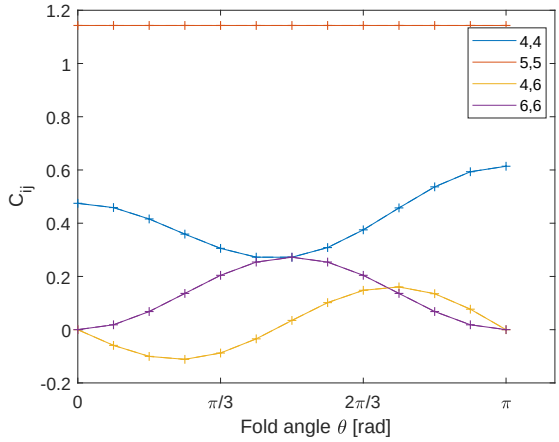

FIGURE 8: Rotational compliance matrix values

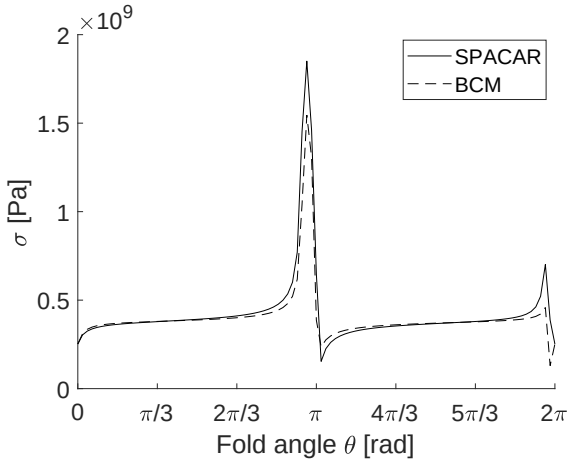

FIGURE 9: Stress comparison between BCM and SPACAR for $u_z = 4$ mm

(BCM) by Awtar et al. [13]. The BCM was numerically solved for two coupled beam elements with appropriate constraints to find the bending moment. The constraints include clamping at the fixed end and a pure translation of 4 mm in z directing with no rotation at the free end. In Fig. 9 the calculated stress can be compared with the equivalent stress results given by SPACAR, which also takes other stresses into account. The figure shows a good agreement and indicates that bending stress has the largest portion in the equivalent stress for this load case.

Optimization of the analytic model. Using the compliance matrix of a single folded leaf spring, the stiffness matrix of the concept with three leaf springs displayed in Fig. 3 can be constructed. Grootens [14] presented equations for transforming compliance matrices to a new translated and rotated coordinate system. The inverse of the transformed compliance matrices will be summed to obtain the full stiffness matrix:

$$K = \sum_{i=1}^{n} (T_i S T_i')^{-1} \tag{17}$$

Where S is the compliance matrix, T is the transformation matrix and n is the number of leaf springs. Optimiziation using the Matlab algorithm `fmincon` yields the following dimensions:

$$\begin{aligned} L_a &= 23.5\,mm \\ L_b &= 53.5\,mm \\ w &= 44.5\,mm \\ t &= 0.30\,mm \\ \theta &= 3.1456\,rad \end{aligned}$$

The corresponding stiffness and eigenfrequencies are:

$$\begin{aligned} Kx, Ky &= 7.02 \cdot 10^7\, N/m \\ Kz &= 1.72 \cdot 10^3\, N/m \\ Krx, Kry &= 1.54\, Nm/rad \\ Kz &= 3.03 \cdot 10^7\, Nm/rad \\ \omega_3 &= 6.6\, Hz \\ \omega_4 &= 833\, Hz \end{aligned}$$

In the undeflected position this is a feasible result. The result for θ immediately stands out since it is almost equal to π, meaning the results converged to a flat flexure strip with length $L_a + L_b$. This is caused by the minimum in the stress plot in Fig. 9. To constrain the optimization, the stress in the deflected situation is taken into account. However, the decrease in stiffness due to deformation is not considered, which would require the thickness to be larger. In this case the stress will exceed the yield limit, which could be relieved with a different fold angle. To investigate this, numerical analyses covering the entire range of motion are required. A fold angle θ is chosen based on Figs. 7 and 8. The compliance in z-direction ($C_{3,3}$) is at its maximum for $\theta = \pi$. However, a shortening effect occurs which should be released by a compliance in x-direction ($C_{1,1}$) is constrained at that angle. Therefore a fold angle of $\pi/2$ is a compromise to allow both translations. The desired compliance around the y-axis ($C_{5,5}$) is independent of the fold angle, where for the x-axis ($C_{4,4}$) it is not. A minimum occurs at $\pi/2$ which is unfavourable but tolerated since a parasitic compliance coupling x- and z-rotation is zero at that angle. In conclusion, a fold angle of $\pi/2$ rad is the best and will be used in upcoming concepts.

Simulation Trajectory

The requirements on stiffness and stress have to be met for the entire range of motion, so during simulation a worst case trajectory must be covered. A translational stroke along the z-axis of $\pm$ 4 mm and a rotational stroke of $\pm$ 0.04 rad is applied such that the entire workspace is reached. The rotation axis must be chosen such that the worst case scenario for stiffness drop and stress occurs. To find the optimal rotation axis analytic equations are used.

Only the horizontal parts of the leaf springs from Fig. 3 are observed. The vertical parts are assumed to be rolling supports with no longitudinal stiffness and infinite lateral stiffness. This is not an entirely accurate assumption since the vertical part of a folded leaf spring can twist. However, it is justified since only the stiffness drop due to deflection is observed. Using analytic equations by Nijenhuis et al. [15] for lateral support stiffness of a leaf spring in a 3D deformation the rotation axis that has the highest impact on support stiffness can be found. Differentiating the lateral error motion relation to the lateral force yields an expression for the compliance in that direction:

$$S_y(\phi_x,\phi_y,u_z) = \frac{L^3}{3EI_z} + \frac{L^3}{180EI_y}\phi_x^2 + \frac{L^3}{GJ}\{\phi_y\ u_z/L\}\begin{bmatrix}13/1260 & -1/105\\ -1/105 & 3/35\end{bmatrix}\begin{Bmatrix}\phi_y\\ u_z/L\end{Bmatrix} \tag{18}$$

The axis around which the rotational deformation is applied is prescribed by an angle θ_a with respect to the x-axis. The prescribed rotational deformation ϕ must be split into torsional rotation ϕ_x and bending rotation ϕ_z for each leaf spring with index i:

$$\phi_{xi} = cos(\theta_i - \theta_a)\phi \tag{19}$$

$$\phi_{yi} = sin(\theta_i - \theta_a)\phi \tag{20}$$

where θ_i is the angle of leaf spring i with respect to the global x-axis. This is illustrated in Fig. 10. The total deflection in z-direction is a combination of pure z-translation and tilting around the rotation axis due to the offset of the leaf springs.

$$u_{zi} = u_z + r_{ls}\sin(\theta_i - \theta_a)\sin(\phi) \tag{21}$$

The lateral stiffness of each leaf spring is different due to different deformations and is determined by:

$$K_i = \frac{1}{S_y(\phi_{xi},\phi_{zi},u_{zi})} \tag{22}$$

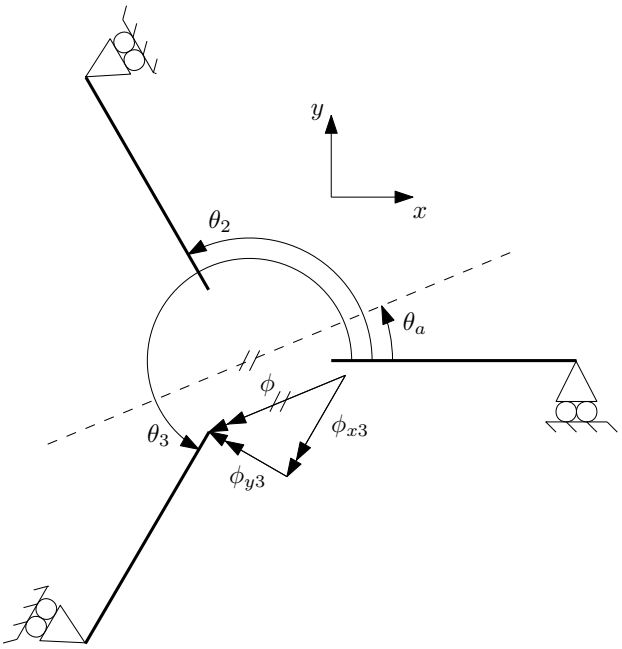

FIGURE 10: Schematic illustration of rotation ϕ around an axis angled at θ_a.

The total support stiffness of multiple radially arranged leaf springs along an axis at an angle θ with respect to the global x-axis is:

$$K(\theta) = \sum_{i=1}^{n} K_i \sin(\theta_i - \theta)^2 \tag{23}$$

By observing the minimum of Eq. (23) for all rotation axis angles θ_a, the rotation axis direction that yields the largest stiffness drop can be found. In Fig. 11a the stiffness distribution from Eq. (23) is plotted for $\theta_a = \pi/2$.

In Fig. 11b the minimum stiffness is plotted against the rotation axis angle for the case of three radially arranged leaf springs. The number of periods is equal to the number of leaf springs. From this figure can be concluded that the first stiffness minimum occurs at a rotation axis angled $\pi/2$ with respect to the x-axis.

As a measure for the occurring stress, bending en torsion stresses per leaf spring are calculated using the load-displacement relations from Nijenhuis et al. [15].

$$\sigma = \frac{E(3u_y - 2L\phi_y)t}{L^2} \tag{24}$$

$$\tau = \frac{G\phi_x w}{2L} \tag{25}$$

The maximum Von Mises equivalent stress is plotted in Fig. 12.

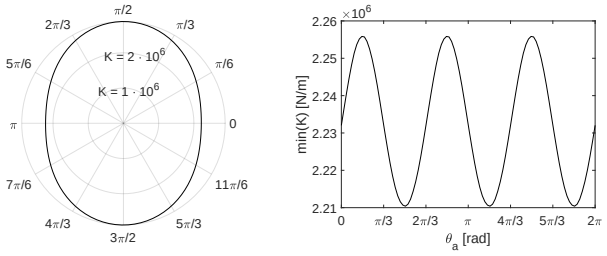

(a) (b)

FIGURE 11: (a) Stiffness distribution for $\theta_a = \pi/2$. (b) Minimum support stiffness for 3 leaf springs.

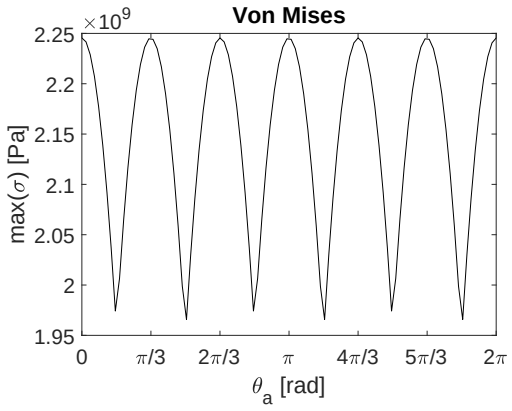

FIGURE 12: Maximum Von Mises stress for 3 leaf springs.

The angles for maximum stress do not match the angles for minimum support stiffness. At $\pi/2$ the stiffness and stress are both at a minimum. Because the variation in stiffness is much smaller than the variation in stress, a rotation axis $\theta_a = 0$ rad from the x-axis is chosen. At this θ_a, the stress is at a maximum and the stiffness is at the average value. If a higher number of leaf springs is used, the stiffness distributions transitions from elliptic to circular, making the stiffness minimum less dependent on the rotation axis orientation. Also, the difference between minimum and maximum stress reduces, but independent of the number of leaf springs a maximum remains at $\theta_a = 0$.

Multi-Body Modeling and Analysis

For more complex concepts and more detailed analyses, parametric models are created using the flexible multi body software SPACAR [16]. The software uses 3D finite beam elements. Compared to FEM analyses only a small amount of elements is required to obtain accurate results, which results in fast simulation times. This is favourable since optimizations require many evaluations of the model. To model the flexible sections, BEAMW elements implemented by Jonker [17] are used, which take constrained warping into account.

The end-effector connecting the flexures in the centre is modelled with massless rigid beam elements. To correctly model the dynamic behaviour a lumped mass with values from Table 1 is applied to the centre node.

During each function evaluation of the optimization algorithm, the parametric model is evaluated by a number of SPACAR analyses. First, a static simulation is conducted covering the translational trajectory in z-direction [18]. In this analysis the end-effector is constrained in all but the z-direction. The only eigenfrequencies found in this analysis are internal modes of leaf springs as the position of the end-effector is prescribed (and not free to move). To obtain the eigenfrequencies of the unconstrained system in a deflected state, a linearisation is conducted around the obtained static equilibrium solution of the first simulation with with the position of the end-effector no longer prescribed [19]. Therefore, during this analysis the driving constraints are removed so the eigenfrequencies of the end-effector can be extracted for the entire trajectory.

Symmetry. To further decrease the simulation time the rotational symmetry of the concepts is exploited. By analysing one leaf spring, the properties of the entire mechanism can be reconstructed. Each leaf spring has the same shape, but not the same deformation under rotational deflection. Therefore, only the translational stroke can be used during previously described SPACAR runs. The drop in support stiffness due to tilting is relatively small and can be accounted for by increasing the desired support stiffness during optimization. Unfortunately, the occurring stresses caused by tilting are highly dependent on the geometry and cannot be compensated for by a lower constraint value in the optimization. To find the correct maximum stress an additional SPACAR run is executed where translation and tilt are applied to a single leaf spring. This causes additional simulation times but does not exceed the gained reduction by using symmetry.

To ensure that the single analysed leaf spring follows the same path as the full mechanism would, additional constraints have to be added explicitly that would otherwise be imposed by the other leaf springs. Translation of the end-effector in the xy-plane is constrained in all analyses and rotations are all either constrained or prescribed. This blocks parasitic displacements and pivot shifts at the end-effector, which are necessary during symmetry analyses, but not entirely realistic. Therefore, after the optimization the full mechanism is analysed without additional constraints on the end-effector to validate the results.

Postprocessing. The data from the simulation of a single leaf spring is postprocessed to obtain the performance of the full mechanism. The compliance matrix of a single leaf spring evaluated in the point of symmetry is used to determine

the stiffness properties of the entire mechanism.
Similar to the method in the analytical model section, the stiffness matrix of the entire mechanism can be calculated by transforming the compliance matrix of a single leaf spring with Eq. (17).

A difference between 'end-effector-eigenfrequencies' (ω^e) and 'internal-eigenfrequencies' (ω^i) is made. The first are eigenfrequencies concerning displacement of the end-effector, related to the stiffness matrix at the end-effector from Eq. (17). Those are calculated by a generalized eigenvalue analysis of the stiffness and mass matrix at the end-effector. The symmetry point is also the end-effector's centre of mass, so the mass matrix is diagonal with values from Table 1. A total of 6 eigenfrequencies can be found this way. The internal eigenfrequencies regarding vibrations of a single flexure follow directly from the SPACAR analysis and need no postprocessing.

Optimization

The parametric SPACAR models are optimized using the gradient free Nelder-Mead optimization algorithm [20]. Modifications by Naves et al. [21], being adaptive objective functions with penalty constraints and constraint interpolation, are used to improve the performance. Since it is known to work well with a limited number of parameters and not all derivatives of the system are available, this algorithm is chosen. Each concept has a specific parameter vector $\boldsymbol{p}$ for which optimal values have to be found. Although the requirements on the mechanism are defined using stiffness values, optimizing using frequencies is favourable since they are independent of direction so less constraints are required. The desired end-effector-eigenfrequencies are listed in Table 4. It is common practice to optimize the first unwanted eigenfrequency [14] [22], which would be end-effector-eigenfrequency ω_4^e. However, in this paper the support stiffness is of major interest. Therefore, satisfying the ω_4^e constraint is enforced and ω_3^e, which is the highest desired eigenfrequency, is minimized. Hence, the cost function is:

$$\mathcal{F} = max(\omega_3(\boldsymbol{p}, u_z, \theta_x)), \quad \begin{array}{l} \forall u_z \in [-u_{max}, u_{max}], \\ \forall \theta_x \in [-\theta_{max}, \theta_{max}] \end{array} \tag{26}$$

To direct the optimization to a feasible solution a number of constraints and boundary conditions are applied. In Table 2 the boundary conditions are listed that apply to the parameter vectors. These values are based on the build volume, material and production methods. The width at the end-effector w_1 is dependent on the number of leaf springs n_{ls} and the radius r_0 at which they are connected. The horizontal length which is equal to L_b for concept 1 and equal to the sum of the building block lengths for concept 2 and 3, is constrained by the build volume.

TABLE 2: Design parameter boundary conditions

parameter	min	max
$L_{horizontal}$	5 mm	150 mm
w_1	5 mm	$2r_0 \tan(\pi/n_{ls})$
w_n	5 mm	80 mm
t	0.2 mm	5 mm

TABLE 3: Optimization constraints

parameter		value
σ	$\leq$	600 Mpa
$min(\omega_4^e)$	$\geq$	872 Hz
$\frac{min((\omega_4^e)^2)}{max((\omega_4^e)^2)}$	$\geq$	0.5
$min(\omega_1^i)$	$\geq$	250 Hz

Constraints applied to the results from the function evaluations are listed in Table 3. The constraints are enforced using penalties on the cost function. The selected material is STAVAX® [23], which is a stainless tool steel with a maximum yield stress off 1360 MPa and a fatigue limit of 600 Mpa. To satisfy the support stiffness requirements, a penalty constraint is applied to ω_4^e. Preliminary simulations showed that the xy-plane stiffness is critical and rz stiffness is easily satisfied with the existing concepts. Therefore the constraint is set to 870 Hz. The difference in frequency between piston and tip-tilt motion is disregarded initially. This will only become relevant when ω_3^e is satisfactory.

CONCEPT GENERATION

In this section multiple concepts are presented. The following concepts evolve from a base concept to which various levels of complexity and over constraints are added.

Concept 1

Concept 1a. This concept is the basic setup of three prismatic folded leaf springs as described in the requirements section. The model of the leaf spring is depicted in Fig. 13a. The parameter vector containing four variables is:

$$\boldsymbol{p} = \{L_a, L_b, w_1, t\} \tag{27}$$

TABLE 4: end-effector-eigenfrequency requirements

n	axis	ω [Hz]
1	u_z	8.72
2	r_x	17.4
3	r_y	17.4
4	u_z	678
5	u_x	872
6	u_y	872

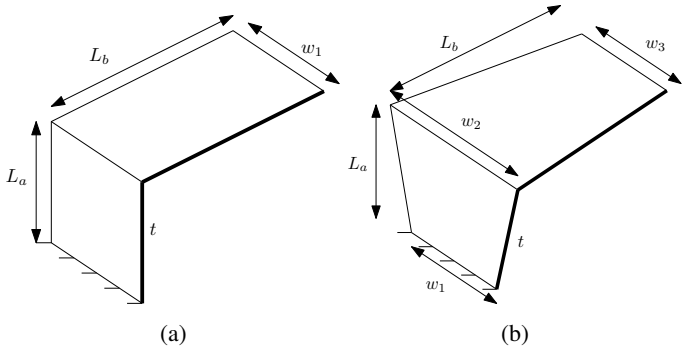

(a) (b)

FIGURE 13: (a) Concept 1a. (b) Concept 1b.

Concept 1b. To improve Concept 1a an option for tapered leaf springs is added. The width of the leaf springs is linearly tapered with three width parameters, at the base, fold and end-effector. The performance is expected to improve compared to prismatic folded leaf springs since the optimization of a tapered leaf spring can also converge to a prismatic leaf spring. The parameter vector for this concept consists of six variables:

$$\boldsymbol{p} = \{L_a, L_b, w_1, w_2, w_3, t\} \tag{28}$$

In Fig. 13b the parametric model of a single leaf spring is illustrated.

Concept 1c. Driving stiffness and support stiffness are both closely related to the ratio w/t. If the vertical part of a folded leaf spring is not taken into account, the load displacement

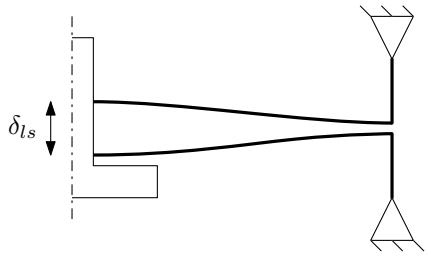

FIGURE 14: Concept 1c.

relations for driving directions are:

$$u_z = F_z \frac{L^3}{12EI_y} = F_z \frac{L^3}{Ewt^3} \tag{29}$$

$$\theta = M_x \frac{L}{GJ} \approx M_x \frac{3L}{Gwt^3} \tag{30}$$

The load displacement relation in lateral direction as described by Nijenhuis [24] is

$$\begin{aligned} u_y &= F_y\left(\frac{L^3}{12EI_z} + \frac{L}{k_z GA} + \frac{L}{28GJ}u_z^2\right) \\ &\approx F_y\left(\frac{L^3}{Ew^3t} + \frac{L}{k_z wt} + \frac{3L}{28Gwt^3}u_z^2\right) \end{aligned} \tag{31}$$

For a high lateral support stiffness and low driving stiffness, a high w/t ratio is desired. However, a torsion related stiffness drop occurs that requires a low w/t ratio to reduce its effect. A solution is to add an additional set of three folded leaf spring which will be placed at an offset to the first set. This is illustrated in Fig. 14. By maintaining the folds of the leaf springs coplanar the constraint space remains satisfied. This modification enables a smaller stiffness drop so a lower support stiffness can be used. Because the support stiffness is related to the driving stiffness, this will also decrease. The parameter vector from concept 1b is augmented with one variable, the offset.

$$\boldsymbol{p} = \{L_a, L_b, w_1, w_2, w_3, t, \delta_{ls}\} \tag{32}$$

Concept 2

The horizontal part of the leaf spring mainly accounts for the deflection required for a stroke, where the vertical part accounts for the shortening effect caused by the stroke. The stiffness of the vertical part has an influence on the drive stiffness of the end-effector. To further reduce this drive stiffness, the vertical and horizontal part are designed separately. The vertical part is modelled as a straight guidance consisting of two parallel leaf

springs, as illustrated in Fig. 15. When modelling the horizontal part, the straight guidance is assumed to have infinite support stiffness, zero driving stiffness and zero parasitic motion. Zero driving stiffness can be achieved by balancing, for example by exploiting post-buckled behaviour of leaf springs as described by Soemers [1].

In Fig. 16 a schematic model can be found. This setup imposes a number of overconstraints. Where a single folded leaf spring has one Degree of Constraint (DoC) and five DoFs, this mechanims constrains an additional DoF. By implementing it 3 times, 3 overconstraints are created. The rotation around z is overconstrained twice and translation in the xy-plane is overconstrained once.

For the topology generation of the horizontal part a building block method is adopted. Naves et al. [21] previously described such a method for parallel systems where all building blocks release the same DoF. In this paper the building blocks are connected in a serial chain where the entire system has to release at least three DoFs. The building blocks and corresponding parameter vectors are:

Leaf spring (LS): $\boldsymbol{p} = \{L, w, t\}$
Compliant revolute joint (CR): $\boldsymbol{p} = \{L, w, t_1, h, t_2\}$ [25]
Torsionally reinforced leaf spring (TRLS): $\boldsymbol{p} = \{L, w, t, h\}$ [21]

A fourth rigid building block exists in the case one of the building blocks above converges to a high thickness and width. The total parameter vector is a concatenation of three sub-parameter vectors from the building blocks:

$$\boldsymbol{p} = \{\boldsymbol{p}_1, \boldsymbol{p}_2, \boldsymbol{p}_3\} \tag{33}$$

To find the optimal topology, a fast optimization method is used that swaps the building blocks and only optimizes a part of the parameter vector that corresponds to the active building block. The building blocks are optimized consecutively, but the performance of the entire system is taken into account. The small number of parameters per optimization run yields a fast convergence. Initial dimensions for the blocks that are not yet optimized have to be chosen. To eliminate the effect of initial dimensions, the loop of consecutive optimization is passed twice. In the current approach there is no strategy for swapping building blocks other than trying all possible combinations. This is feasible for a limited number of different building blocks. Three different topologies resulted from this method, which are listed in Table 5.

In the above-mentioned method, only one width parameter per building block is used. This implies that these blocks are prismatic. It is desirable to use tapered building blocks for a smooth transition between the blocks. This adds a width parameter and implies sharing the width parameters between building block parameter vectors. Consecutive optimization of the building blocks as described above does not work any more in this case, so the entire parameter vector is optimized simultaneously for the final design.

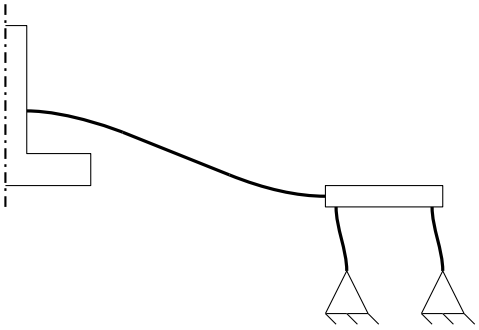

FIGURE 15: Concept 2.

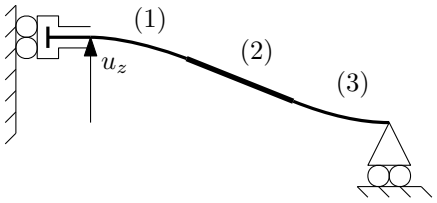

FIGURE 16: Concept 2 model.

TABLE 5: Block configurations for concept 2

Concept	Block 1	Block 2	Block 3
2a	LS	LS	LS
2b	LS	CR	LS
2c	TRLS	CR	TRLS

Concept 3

This concept concerns modifications of the previous concept, where the determined optimal topology is used as a starting point. The alterations are: (a) adding more flexures in parallel, (b) creating an offset between two layers of leaf springs at the end-effector and (c) creating an offset at the outer radius.

Concept 3a. By increasing the number of leaf springs, the number of over constraints also increases. By over constraining the support stiffness can increase substantially, but it can introduce additional stress when not properly assembled. This problem also occurs with non-uniform expansion due to heat or when large deformations are applied. The performance of this

TABLE 6: Optimization results

Concept	ω_3^e [Hz]	ω_4^e [Hz]	ω_1^i	σ [Mpa]	$(\Delta\omega_4^e)^2$
1a	167	871	368	615	0.90
1b	132	868	357	544	0.88
1c	135	883	659	576	0.86
2a	44.0	886	311	624	0.77
2b	66.6	901	357	576	0.71
2c	136	878	426	917	0.84
3a5	29.1	871	272	600	0.82
3a6	26.7	887	302	543	0.87
3a7	25.5	871	365	528	0.80
3b	48.2	880	347	595	0.82
3c	25.9	876	251	546	0.81

concept is investigated for 5, 6 and 7 flexures, denoted as concept 3a5, 3a6 and 3a7 respectively.

Concept 3b. Similarly to concept 1c, creating two layer of leaf springs at an offset to distribute the support stiffness could be favourable. The horizontal leaf springs will be pre-curved in an s-shape and connected to the end-effector with an offset. This makes overlap possible thus increasing the maximum width at the end-effector.

Concept 3c. This concept is similar to concept 3b, with the only modification being the location of the offset. In this case the connections at the end-effector are in the same plane and the offset is applied at the straight guidance.

$$\boldsymbol{p} = \{\boldsymbol{p}_1, \boldsymbol{p}_2, \boldsymbol{p}_3, \delta_{ls}\} \tag{34}$$

RESULTS & DISCUSSION

For each concept the optimizations are executed using the method explained previously. Using these results the best concept can be chosen for detailed design and validation. In Table 6 the results of the performance criteria for each concept are listed. The corresponding parameters and illustrations can be found in Appendix B.

The concepts are optimized for a minimal ω_3^e with the constraints from Table 3. The optimal results are expected to exactly meet the constraints for ω_4^e and σ. However, this is not the case because the symmetry of the concepts is exploited during optimization. As explained in the Method section, additional boundary conditions on the end-effector are necessary if only one flexure is analysed. The boundary conditions required for a single leaf spring to follow the test trajectory are infinitely stiff, where in the full mechanism they are not because they are imposed by other leaf springs. This causes parasitic displacements of the end-effector to be constrained during optimization, where in the final full simulation they are released, yielding different results.

During the optimization of concept 1a no feasible results were found. Either the ω_3^e or σ constraint was violated in each result. Tapering the leaf springs of concept 1a to obtain concept 1b yields a significant drop of the third eigenfrequency. Adding an inverted layer of leaf springs in concept 1c does not increase $(\Delta\omega_4^e)^2$ which was expected. Furthermore, only the internal eigenfrequencies significantly increase with respect to concept 1b.

Within concept 2, concept 2a clearly performs best. Compared to 2b and 2c it reaches the lowest ω_3^e. The centre building block converges to a long reinforcement with respect to the other two building blocks. Torsion is accounted for by building block 1 and bending by building block 1 and 3 simultaneously. Concept 2c suffers severely from the effect of changing boundary conditions as described above. Therefore it has a high stress and can not be compared properly.

To obtain the results for concepts 3a-c, the building block topology from concept 2a is used. It is clear that increasing the number of flexures from 3 to 5, 6 or 7 has a positive effect on the results. The decrease of ω_3^e is caused by thinner flexure strips compared to concept 2a. The effect of using more than 5 flexures is mainly limited to a lower stress and higher internal eigenfrequency, but does not affect ω_4^e significantly. Some decrease of ω_3^e is observed between 5 and 6 flexures, but this small compared to other modifications. Introducing an offset at the end-effector between two sets of 3 flexures has no positive effect. This is obvious when compared to concept 3a6, which has the same lay-out without offset. Due to limitations in the simulation, a minimum offset of 1 mm was set. The offset converged to a value of 1.19 mm, which is close to the minimum. $(\Delta\omega_4^e)^2$ did not increase by introducing an offset and ω_3^e also performs worse. The model of Concept 3c requires no minimum offset and converges to 0.66 mm. This also suggests an offset is not favourable and it is confirmed by the similarity of the result with concept 3a6.

Summarizing, Concepts 3a yield the best results. To minimize the number of over constraints, concept 3a5 is chosen as the final concept. An additional advantage of this concept is the prime number of flexures which creates no additional symmetry lines. In Fig. 17 a visualization of the SPACAR model is displayed.

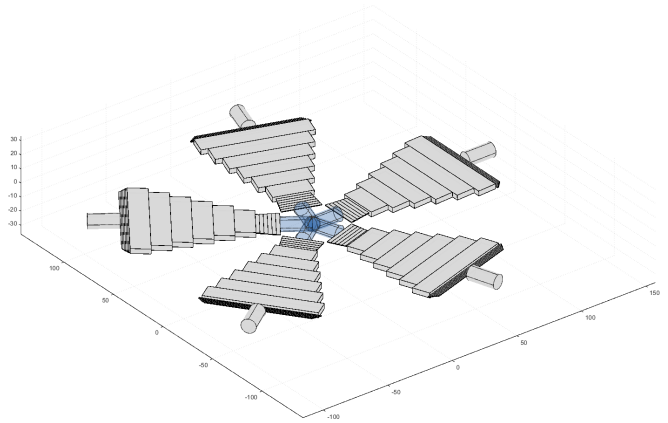

FIGURE 17: SPACAR model

Validation

With the optimal parameter set an ANSYS model is constructed from shell elements to compare the result with SPACAR. The SHELL181 element is used because it well suited for large rotations and strains in non-linear analyses. To couple and constrain the flexures Multipoint Constraint elements (MPC184) are used. In the centre a MASS21 element is placed to model the end-effector. To obtain the same data for the entire stroke, i.e. eigenfrequencies and stiffness matrix, a linear perturbation analysis is executed. Similarly to the SPACAR analysis, first a non-linear static analysis is run to follow the trajectory. Next, constraints defining the trajectory are removed and linear perturbation analyses are run by restarting the simulation in each substep of the static analysis consecutively. To find the unconstrained eigenfrequencies, a modal analysis type is used in the restart. Finding the stiffness at the end-effector requires converting the deflected system into a superelement with a master node at the end-effector position. Restarting the analysis in substructure mode calculates the 6x6 stiffness matrix of the superelement.

In Table 7 the first 16 vibration modes are listed in the neutral position. Low frequency behaviour is sufficiently accurate which can also be seen in Fig. 18 where the first three eigenfrequencies over the entire stroke are plotted. For the higher frequencies, an increasing difference between SPACAR and ANSYS occurs, as plotted in Fig. 19. The different trend of the eigenfrequency towards the end of the stroke stands out, which is caused by a difference in mode shape between SPACAR and ANSYS.

From Fig. 21 can be concluded that there is a difference in calculated stress between ANSYS and SPACAR. From the SPACAR stress calculations it is known that warping and anticlastic bending are not taken into account. The high stress produced by ANSYS is concentrated at the clamped nodes, as displayed in Fig. 22. The overall stiffness properties of the system

TABLE 7: First 16 eigenfrequencies

	SPACAR		ANSYS	
1	15.14	ω_1^e u_z	14.35	ω_1^e u_z
2	23.71	ω_2^e r_x	2443	ω_2^e r_x
3	23.71	ω_3^e r_y	24.43	ω_3^e r_y
4	271.6	ω_1^i Bending	284.8	ω_1^i Bending
5	271.6	ω_2^i Bending	284.8	ω_2^i Bending
6	277.1	ω_3^i Bending	290.5	ω_3^i Bending
7	277.1	ω_4^i Bending	290.5	ω_4^i Bending
8	286.3	ω_5^i Bending	297.2	ω_5^i Bending
9	771.8	ω_6^i Torsion	745.5	ω_4^e u_x
10	771.8	ω_7^i Torsion	745.5	ω_5^e u_y
11	771.8	ω_8^i Torsion	1223	ω_6^i Torsion
12	771.8	ω_9^i Torsion	1223	ω_7^i Torsion
13	771.8	ω_{10}^i Torsion	1223	ω_8^i Torsion
14	842.8	ω_4^e u_x	1223	ω_9^i Torsion
15	842.8	ω_5^e u_y	1223	ω_{10}^i Torsion
16	1503	ω_6^e r_z	1493	ω_6^e r_z

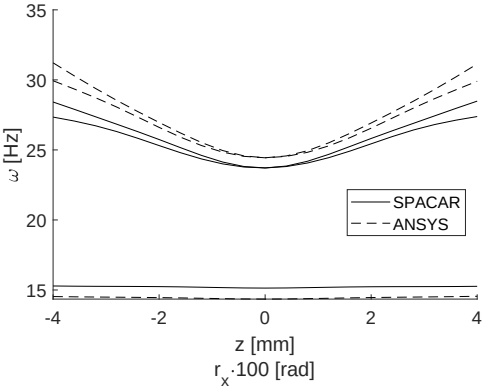

FIGURE 18: end-effector mode 1, 2 and 3

are slightly underestimated by SPACAR according to the plots in Fig. 20. Therefore, another design iteration could be made to reduce the stiffness and stress in the mechanism.

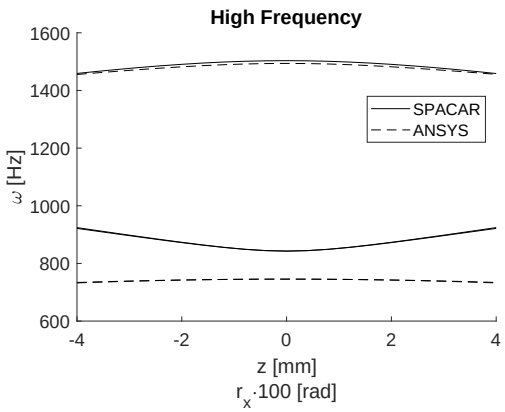

FIGURE 19: end-effector mode 4, 5 and 6

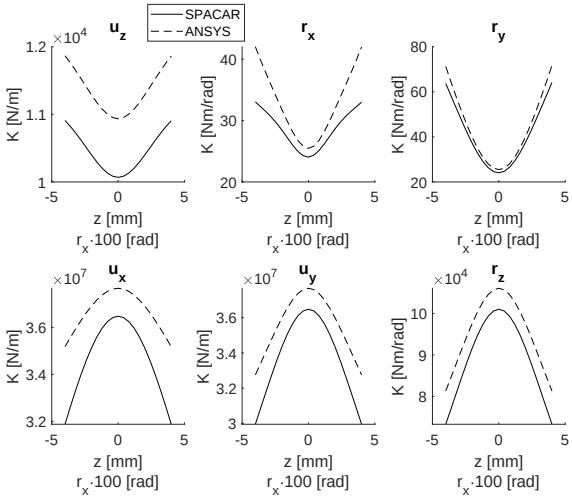

FIGURE 20: Stiffnesss comparison

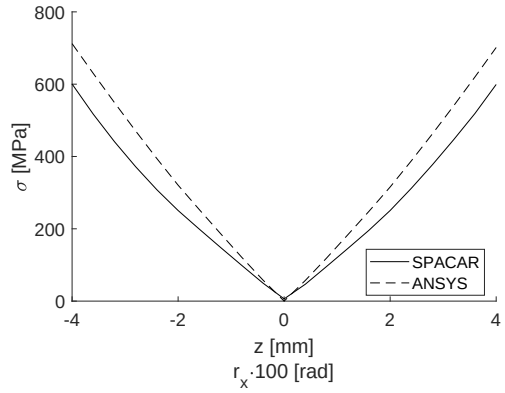

FIGURE 21: Stress

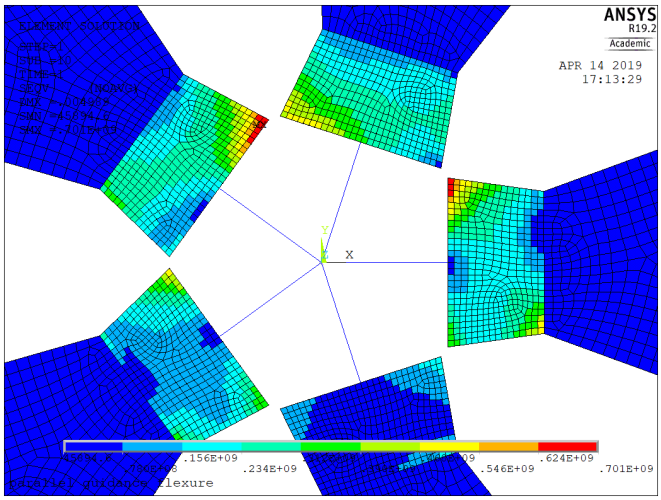

FIGURE 22: Stress concentration for $u_z = 4$ mm and $r_x = 0.04$ rad.

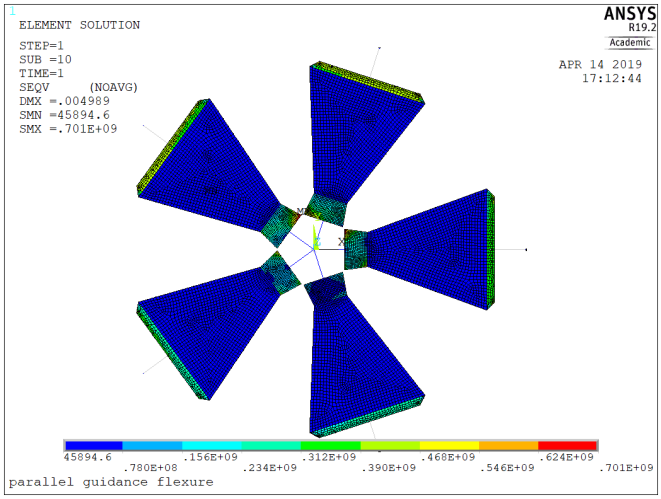

FIGURE 23: Von Mises stress

Pivot shift

Although no requirements were set on pivot shift, it is an important factor in flexure mechanism performance. In Table 8 the pivot shift in x- and y-direction are listed as calculated in SPACAR and ANSYS. Similar values are obtained by both methods. The calculated values are approximately 0.1 % of the total deflection, which is small compared to a conventional straight guidance or cross spring pivot.

TABLE 8: Pivot shift

	SPACAR	ANSYS
$\delta x\ [mm]$	$-1.07 \cdot 10^{-4}$	$-1.96 \cdot 10^{-4}$
$\delta y\ [mm]$	$-6.73 \cdot 10^{-3}$	$-6.79 \cdot 10^{-3}$

CONCLUSION

The desired specifications for a specific TTP mechanism can be approached by improving a base concept of three folded leaf springs. An analytical model shows that the requirements can be met in the equilibrium position. To meet the requirements for the entire range of motion more extensive multi-body analyses are required. Tapering the flexures has a positive effect on the performance of the mechanism. Moreover, using building blocks to enable varying width and thickness through the leaf spring yield better results. To decrease the simulation time during optimization, an optimal simulation trajectory was determined analytically. Through this trajectory the best and worst case scenarios within the workspace are covered. Exploiting the symmetry of the mechanism by simulating a single repetitive element proved to be a good method to reduce simulation time. Through optimization was found that a circular pattern of five tapered flexure elements consisting of three segments is the best result considering driving stiffness and overconstraints. The flexure elements need to be supported by an appropriately designed straight guidance with minimal driving stiffness. The last desired eigenfrequency is reduced to 29.1 Hz, where 17.4 Hz was required. Validation of this result by ANSYS yields a comparable value of 31 Hz. Since the stress and support stiffness computed by ANSYS exceed the requirements, a re-iteration of the design process could result in a design closer to the requirements.

RECOMMENDATIONS

The fold angle of the leaf spring was chosen based on the compliance matrix graphs from the analytical model. This model is only valid in the equilibrium position so only limited conclusions can be drawn. Adding the fold angle to the parameter vector of concept 1 could improve its results.

The stress calculation in SPACAR does not take warping and anticlastic bending into account, which could alter the optimization results. Since this is a known and recurring effect, it could be corrected for by decreasing the maximum stress during optimization.

Validity of tapered leaf springs only tested for low frequency behaviour. From validation results it is apparent that high frequency behaviour is significantly different.

A straight guidance with high support stiffness and low driving stiffness will have to be designed. By balancing the driving stiffness can be decreased. A possible method consists of implementing a leaf spring in post-buckled state to a parallel guidance [1]. If designed properly, the negative stiffness could counteract the driving stiffness.

REFERENCES

[1] Soemers, H., 2011. *Design principles for precision mechanisms*. T-Pointprint.

[2] Koster, M. P., 2005. *Constructieprincipes voor het nauwkeurig bewegen en positioneren*. PPI Uitgeverij.

[3] Zhu, Y., Liu, W., Jia, K., Liao, W., and Xie, H., 2011. "A piezoelectric unimorph actuator based tip-tilt-piston micromirror with high fill factor and small tilt and lateral shift". *Sensors and Actuators A: Physical,* ***167***(2), jun, pp. 495–501.

[4] Wu, L., Dooley, S., Watson, E. A., McManamon, P. F., and Xie, H., 2010. "A tip-tilt-piston micromirror array for optical phased array applications". *Journal of Microelectromechanical Systems,* ***19***(6), dec, pp. 1450–1461.

[5] Tapos, F. M., Edinger, D. J., Hilby, T. R., Ni, M. S., Holmes, B. C., and Stubbs, D. M., 2005. "High bandwidth fast steering mirror". In Optomechanics 2005, Vol. 5877, International Society for Optics and Photonics, p. 587707.

[6] Lee, K.-M., and Arjunan, S., 1992. "A three degrees of freedom micro-motion in-parallel actuated manipulator". In *Precision Sensors, Actuators and Systems*. Springer, pp. 345–374.

[7] Pernette, E., Henein, S., Magnani, I., and Clavel, R., 1997. "Design of parallel robots in microrobotics". *Robotica,* ***15***(4), pp. 417–420.

[8] Hao, G., and He, X., 2017. "Designing a monolithic tip-tilt-piston flexure manipulator". *Archives of Civil and Mechanical Engineering,* ***17***(4), sep, pp. 871–879.

[9] Hopkins, J. B., and Culpepper, M. L., 2010. "Synthesis of multi-degree of freedom, parallel flexure system concepts via freedom and constraint topology (fact) – part i: Principles". *Precision Engineering,* ***34***(2), pp. 259 – 270.

[10] van Eijk, J., 1985. "On the design of plate-spring mechanisms". PhD thesis, Technische Hogeschool Delft.

[11] Vlasov, V. Z. V. Z., 1961. *Thin-walled elastic beams*, 2nd ed. rev. and augm. / translated from russian [by y. schectman] ed. Israel Program for Scientific Translations, Jerusalem.

[12] Cowper, G. R., 1966. "The shear coefficient in timoshenko's beam theory". *Journal of applied mechanics,* ***33***(2), pp. 335–340.

[13] Awtar, S., and Sen, S., 2010. "A generalized constraint model for two-dimensional beam flexures: Nonlinear load-displacement formulation". *Journal of Mechanical Design,* ***132***(8), p. 081008.

[14] Grootens, M. E., 2014. "Synthesi and optimization of large stroke flexure hinges". Master's thesis, University of Twente, Drienerlolaan 5, 7522NB Enschede.

[15] Nijenhuis, M., Meijaard, J. P., and Brouwer, D. M., 2018. "A spatial parametric model for the nonlinear stiffness characteristics of flexure strips". In ASME 2018 International Design Engineering Technical Conferences and Computers and Information in Engineering Conference, American Society of Mechanical Engineers, pp. V05AT07A014–V05AT07A014.

[16] Jonker, J., and Meijaard, J., 1990. "Spacar—computer program for dynamic analysis of flexible spatial mechanisms and manipulators". In *Multibody systems handbook*. Springer, pp. 123–143.

[17] Jonker, J. B., 2017. "Implementation of shear deformable thin-walled beam element for flexible multibody dynamics". pp. 141–162. 8th ECCOMAS Thematic Conference on MULTIBODY DYNAMICS 2017, Multibody 2017 ; Conference date: 19-06-2017 Through 22-06-2017.

[18] Meijaard, J. P., 2018. "A method for calculating and continuing static solutions for flexible multibody systems". *Journal of computational and nonlinear dynamics,* ***13***(7), 5.

[19] dr. ir. R. G. K. M. Aarts, d. i. J. P. M., and prof. dr. ir. J. B. Jonker, 2017. *SPACAR user manual*, 2017 ed., Oct.

[20] Nelder, J. A., and Mead, R., 1965. "A simplex method for function minimization". *The computer journal,* ***7***(4), pp. 308–313.

[21] Naves, M., Brouwer, D. M., and Aarts, R. G. K. M., 2017. "Building block based spatial topology synthesis method for large stroke flexure hinges". *Journal of mechanisms and robotics,* ***9***(4), 5.

[22] Wiersma, D. H., Boer, S. E., Aarts, R. G. K. M., and Brouwer, D. M., 2014. "Design and performance optimization of large stroke spatial flexures". *Journal of computational and nonlinear dynamics,* ***9***(1), p. 011016.

[23] UDDEHOLMS AB, 2013. *UDDEHOLM STAVAX® ESR*, 11 ed., May.

[24] Nijenhuis, M., Meijaard, J. P., Mariappan, D., Herder, J. L., Brouwer, D. M., and Awtar, S., 2017. "An analytical formulation for the lateral support stiffness of a spatial flexure strip". *Journal of mechanical design,* ***139***(5), p. 051401.

[25] Trease, B. P., Moon, Y.-M., and Kota, S., 2005. "Design of large-displacement compliant joints". *Journal of Mechanical Design,* ***127***(4), p. 788.

APPENDIX A Tapered Leaf springs

The main advantage of SPACAR is the ability to model a beam with approximately three beam elements. Unfortunately, tapered beam models are not supported so tapered beams must be discretized with prismatic beam elements. This causes the number of elements to rapidly increase which is undesirable. Therefore, the lowest amount of beam elements necessary to accurately model a tapered beam is sought. This is done by analysing a cantilever leaf spring for different taper ratios and different numbers of elements. The taper ratio is defined as

$$TR = \frac{W_1}{W_2} \tag{35}$$

The width of the prismatic beam elements is determined by the width of the tapered leaf spring at the centre of the segment. In Fig. 24 this is schematically displayed.

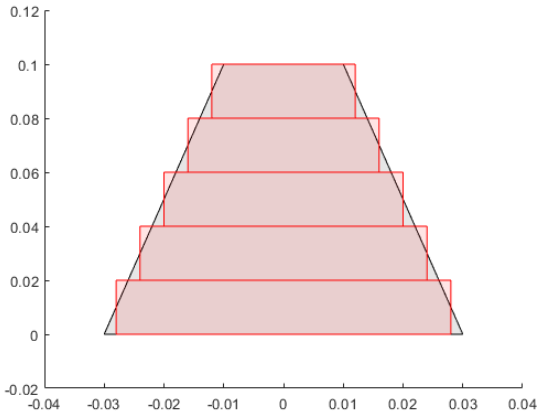

FIGURE 24: Discrete approximation of a tapered leaf spring.

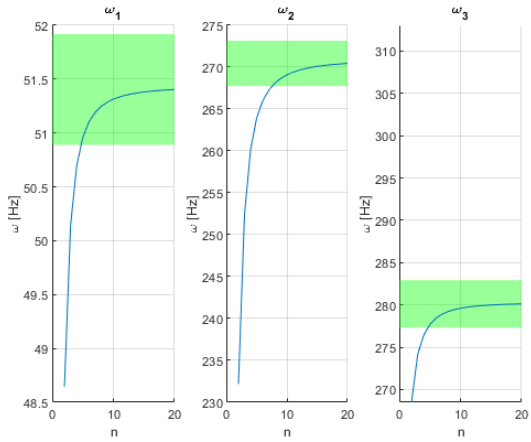

FIGURE 25: Eigenfrequencies versus number of elements for $TR = 0.5$

The number of elements is sufficient if the first 3 eigenfrequencies of the simulation are within 5% of the asymptotic value for a certain taper ratio. The asymptotic value is calculated using a simulation with 20 elements. In Fig. 25 the first 3 eigenfrequencies are plotted versus different numbers of elements for $TR = 0.5$.

The required number of element is dependent on the taper ratio of the leaf spring. For a straight leaf spring three elements are required and this number increases for higher taper ratios. In Fig. 26 a graph can be found for required number of elements for taper ratios between 0.1 and 1.

To complete this appendix the effect of different aspect ratios is observed. The aspect ratio is defined as:

$$AR = \frac{L^2}{S} = \frac{2L}{(W_1 + W_2)} \tag{36}$$

In figure the required numer of elements versus the aspect ratio is plotted for a taper ratio of 1:10, which is the worst case ratio from Fig. 26. It appears that the accuracy is less dependent on aspect ratio than on taper ratio. Only in the worst case with a taper ratio of 1:10 and an aspect ratio of 1, 7 elements are required. A significant dependence on the thickness of the leaf spring is not found.

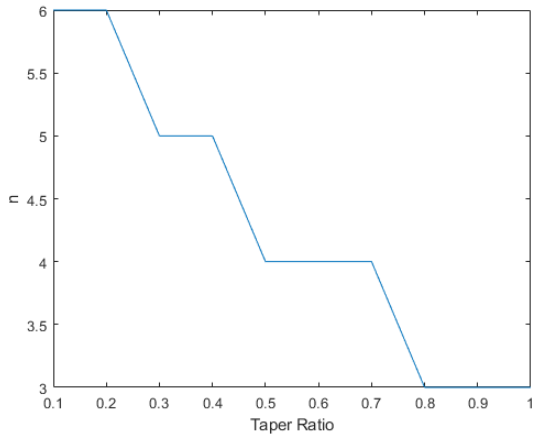

FIGURE 26: Required number of elements for different taper ratios

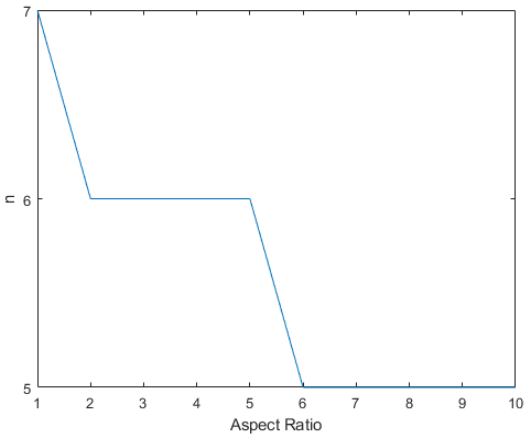

FIGURE 27: Required number of elements for different taper ratios

APPENDIX B Optimization Results

Concept 1a.

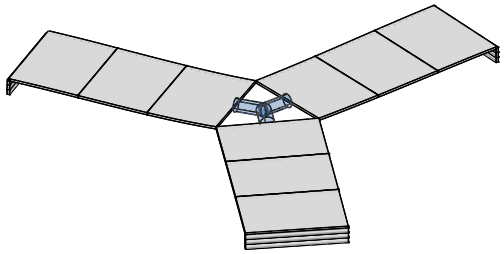

FIGURE 28: SPACAR model

L_a	150
L_b	11.4
w_1	69.3
t	1.73

TABLE 9: Parameters

Concept 1b.

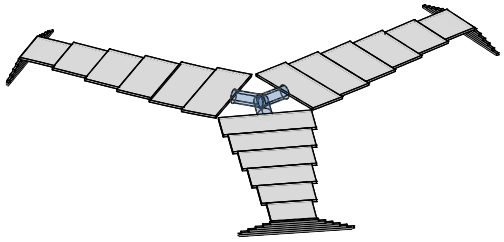

FIGURE 29: SPACAR model

L_a	149
L_b	15.7
w_1	66.4
w_2	27.6
w_3	86.3
t	1.6

TABLE 10: Parameters

Concept 1c.

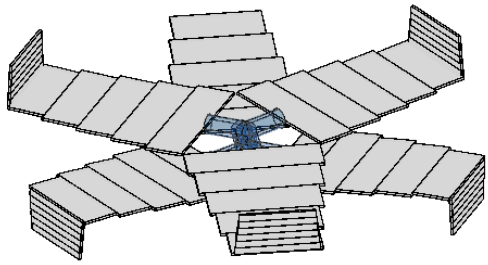

FIGURE 30: SPACAR model

L_a	149
L_b	15.7
w_1	66.4
w_2	27.6
w_3	86.3
t	1.6
δ_{ls}	9.99

TABLE 11: Parameters

Concept 2a.

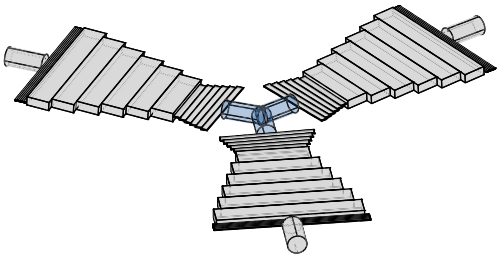

FIGURE 31: SPACAR model

Block	1	2	3
Type	LS	LS	LS
L	21.0	72.3	5.80
w_1	49.4	33.4	79.7
w_2	33.4	79.7	79.9
t_1	0.524	4.78	0.486
t_2	-	-	-
h_1	-	-	-

TABLE 12: Parameters

Concept 2b.

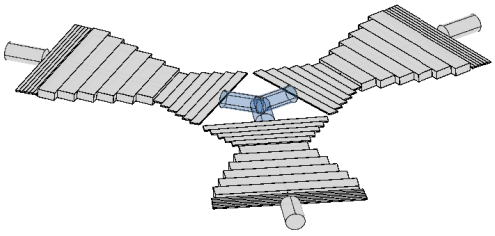

FIGURE 32: SPACAR model

Block	1	2	3
Type	LS	CR	LS
L	31.3	54.9	11.0
w_1	65.9	30.9	76.8
w_2	30.9	76.8	78.3
t_1	0.702	4.79	0.811
t_2	-	0.24	-
h_1	-	2.91	-

TABLE 13: Parameters

Concept 2c.

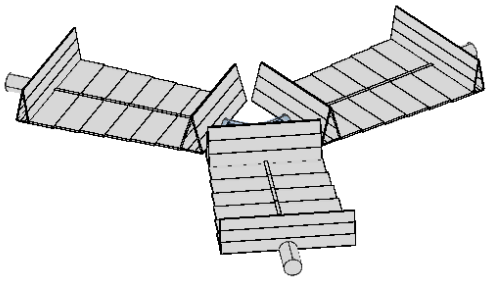

FIGURE 33: SPACAR model

Block	1	2	3
Type	TRLS	CR	TRLS
L	13.0	87.8	7.13
w_1	62.33	62.3	74.5
w_2	-	74.5	-
t_1	0.879	1.19	0.595
t_2	-	1.97	-
h_1	-	3.27	-

TABLE 14: Parameters

Concept 3a5.

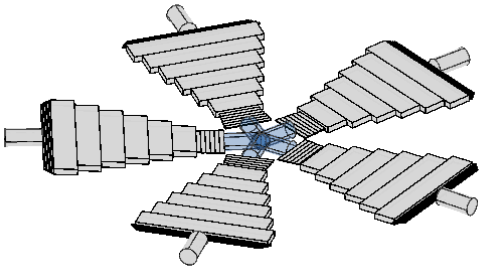

FIGURE 34: SPACAR model

Block	1	2	3
Type	LS	LS	LS
L	12.0	72.4	5.04
w_1	26.2	12.0	77.4
w_2	12.0	77.4	76.5
t_1	0.329	4.71	0.364
t_2	-	-	-
h_1	-	-	-

TABLE 15: Parameters

Concept 3a6.

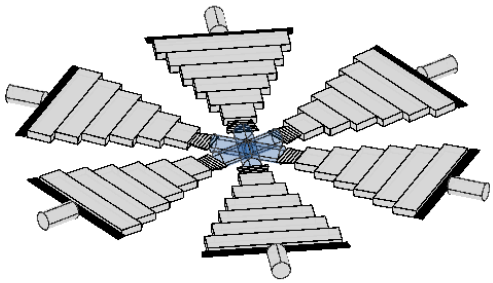

FIGURE 35: SPACAR model

Block	1	2	3
Type	LS	LS	LS
L	11.2	81.5	5.09
w_1	17.21	12.3	77.8
w_2	12.3	77.8	79.5
t_1	0.345	4.21	0.393
t_2	-	-	-
h_1	-	-	-

TABLE 16: Parameters

Concept 3a7.

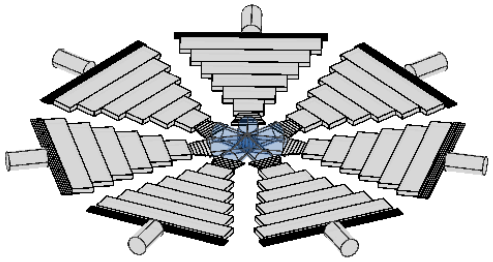

FIGURE 36: SPACAR model

Block	1	2	3
Type	LS	LS	LS
L	10.8	68.5	5.82
w_1	17.8	9.93	78.1
w_2	9.93	78.1	78.3
t_1	0.319	2.72	0.346
t_2	-	-	-
h_1	-	-	-

TABLE 17: Parameters

Concept 3b.

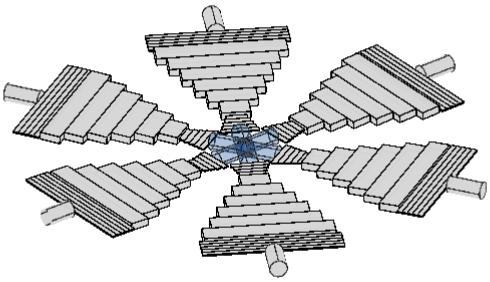

FIGURE 37: SPACAR model

Block	1	2	3
Type	LS	LS	LS
L	17.5	70.8	15.3
w_1	22.9	10.8	79.8
w_2	10.8	79.8	79.9
t_1	0.559	4.36	0.837
t_2	-	-	-
h_1	-	-	-
$\delta_l s$	1.19		

TABLE 18: Parameters

Concept 3c.

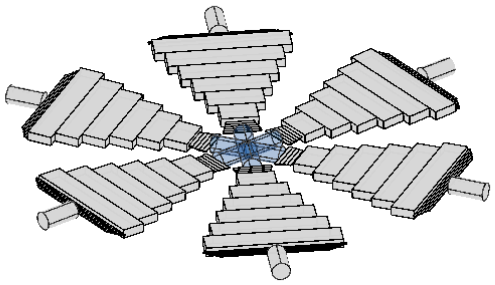

FIGURE 38: SPACAR model

Block	1	2	3
Type	LS	LS	LS
L	11.1	81.7	5.91
w_1	21.3	15.1	79.9.0
w_2	15.1	79.9	58.9
t_1	0.308	4.971	0.381
t_2	-	-	-
h_1	-	-	-
$\delta_l s$			0.662

TABLE 19: Parameters